What is the effect of self-induced pressure waves and their wall reflections on low Reynolds number airfoil flow in wind tunnels?

Bjoern F. Klose*
San Diego State University, San Diego, CA 92182, USA

Geoffrey R. Spedding†
University of Southern California, Los Angeles, CA 90007, USA

Gustaaf B. Jacobs‡
San Diego State University, San Diego, CA 92182, USA

The stability of low Reynolds number airfoil flow in a confined domain, resembling the test section of a wind tunnel, is investigated computationally for a cambered NACA 65(1)-412 compressor blade. Compressible Navier-Stokes simulations of the blade flow at 4° and 8° of incidence are compared for slip-wall and free-stream boundary conditions to evaluate the effect of pressure waves induced by vortex shedding, including the effects of reflections on wind tunnel walls. The domain size, blockage and type of boundary condition are shown to have a substantial impact on the shape of the laminar separation bubble and the wake for an angle of attack of 8° of incidence, while the flow is nearly indifferent to these factors at 4° of incidence. For the former, the interaction of the reflected pressure waves from the walls with the laminar separation bubble at the leading edge of the airfoil drives the shear instability and accelerates the vortex shedding, resulting in a reduction of the laminar separation bubble length. At 4° of incidence, a reoccurring interference pattern in the reflected pressure waves results in local increase and decrease of pressure and skin-friction fluctuations on the airfoil surface, as well as a more irregular vortex shedding. Despite having a strong effect on the flow topology, the wall boundaries change the aerodynamic forces only by 5% at most at these low incidence angles.

I. Nomenclature

C_d	=	drag coefficient
C_f	=	skin friction coefficient
C_l	=	lift coefficient
C_p	=	pressure coefficient
c	=	chord
e	=	internal energy
$\mathbf{F}$	=	flux vector
h_R	=	reverse flow height
M	=	Mach number
N	=	polynomial order
p	=	pressure
Pr	=	Prandtl number
Re	=	Reynolds number
R_T	=	temperature ratio
S	=	Sutherland constant
t	=	time
T	=	temperature
$\mathbf{U}$	=	vector of conserved variables

*Department of Aerospace Engineering, bklose@sdsu.edu
†Department of Aerospace and Mechanical Engineering, geoff@usc.edu
‡Department of Aerospace Engineering, gjacobs@sdsu.edu

u, v, w	=	velocity components
U_R	=	normalized reversed tangential velocity
x, y, z	=	Cartesian coordinates
y^+	=	wall coordinate
γ	=	ratio of specific heats
δ^*	=	displacement thickness
κ	=	thermal diffusivity
ρ	=	density
τ	=	stress tensor
AOA	=	angle of attack
LSB	=	laminar separation bubble
$R_{3.5}$, R_{30}	=	domain radius reference
RMS	=	root mean square

II. Introduction

AIRFOIL flow at low to intermediate Reynolds numbers (Re) is governed by boundary layer separation, reattachment and transition to turbulence – processes that can result in significant and sudden changes of the aerodynamic forces acting on the body. The Reynolds number range $10^4 \leq Re \leq 10^5$ is generally characterized by an initially laminar boundary layer, separation upstream of the trailing edge and transition to turbulence. Depending on where this transition occurs, the flow can reattach and form a laminar separation bubble (LSB). Accurate prediction and control of such flow events is of principal interest when operating aerodynamic devices at moderate Reynolds numbers and high-fidelity benchmark data, both experimental and numerical, are at the foundation to solve this problem.

Capturing the highly non-linear dynamics of the transition process, however, is challenging. Results of experiments collected at different test facilities can differ significantly and experiments at low Reynolds number do not match with DNS results in literature [1]. As remarked many years ago [2], the highly sensitive nature of the complex transitional flows over airfoils at low Reynolds number is likely responsible for continuing disagreements in the otherwise mature field of airfoil and wing aerodynamics for higher Reynolds number.

While the NACA 0012 is a canonical test case for airfoil flows [1], in engineering applications one usually encounters cambered airfoil profiles that generate optimal performance for a given operating condition. In turbomachinery, for example, the blades in axial flow compressors are commonly selected from the NACA 65-series [3, 4] or Eppler series. Compressor blades owe their shape to the adverse pressure gradient against which they operate and their slender profile and small camber allows the flow to remain attached over most of the airfoil under operating conditions. If, however, the flow conditions deviate from the design point, forces induced by boundary layer separation, transition, and reattachment can change rapidly and become difficult to predict [5].

Direct Numerical Simulations (DNS) produce very accurate time and space resolved datasets and are an excellent tool to benchmark the transitional airfoil flow at moderate Reynolds numbers [6]. They are, however, computationally expensive and generally conducted on small domains without accounting for the surrounding environment [7–9]. At low Reynolds numbers, flow separation and transition to turbulence, are particularly sensitive and small changes in the angle of attack can bifurcate the flow field easily and counter-intuitively [5]. For example, acoustic feedback from instability waves originating from the vortex shedding at the trailing edge have been found by Jones et al. [8] to induce a global instability for a NACA 0012 at a Mach number of $M = 0.4$.

In this paper, we investigate the impact of pressure reflections on the instantaneous and mean properties of the transitional flow around a generic compressor blade (NACA 65(1)-412) in a domain with horizontal slip-wall boundaries. Angles of attack of 4° and 8° at a chord-based Reynolds number $Re_c = 2 \times 10^4$ and Mach number $M = 0.3$ are computed using a discontinuous-Galerkin spectral element method [10, 11]. Results from simulations with horizontal slip walls are compared to solutions with free-stream boundaries on the same domain, as well as free-stream computations on a large domain, to isolate the effects of the reflected waves.

III. Governing Equations

A. Conservation Laws

We compute solutions to the compressible Navier-Stokes equations, which can be written in non-dimensional form as the system of equations

$$\partial_t \mathbf{U} + \nabla \cdot \mathbf{F} = 0. \tag{1}$$

In (1), $\mathbf{U}$ represents the vector of the conserved variables,

$$\mathbf{U} = \begin{bmatrix} \rho & \rho u & \rho v & \rho w & \rho e \end{bmatrix}^T. \tag{2}$$

The flux vector $\mathbf{F}$ is split into an advective (superscript a) and a viscous part (superscript v),

$$\nabla \cdot \mathbf{F} = \partial_x \mathbf{F}^a + \partial_y \mathbf{G}^a + \partial_z \mathbf{H}^a - \frac{1}{Re_f} \left(\partial_x \mathbf{F}^v + \partial_y \mathbf{G}^v + \partial_z \mathbf{H}^v \right), \tag{3}$$

where

$$\begin{aligned}
\mathbf{F}^a &= \begin{bmatrix} \rho u & p+\rho u^2 & \rho uv & \rho uw & u(\rho e+p) \end{bmatrix}^T, \\
\mathbf{G}^a &= \begin{bmatrix} \rho v & \rho vu & p+\rho v^2 & \rho vw & v(\rho e+p) \end{bmatrix}^T, \\
\mathbf{H}^a &= \begin{bmatrix} \rho w & \rho wu & \rho wv & p+\rho w^2 & w(\rho e+p) \end{bmatrix}^T,
\end{aligned} \tag{4}$$

$$\begin{aligned}
\mathbf{F}^v &= \begin{bmatrix} 0 & \tau_{xx} & \tau_{yx} & \tau_{zx} & u\tau_{xx}+v\tau_{yx}+w\tau_{zx}+\dfrac{\kappa}{(\gamma-1)\,PrM_f^2}T_x \end{bmatrix}^T, \\[2mm]
\mathbf{G}^v &= \begin{bmatrix} 0 & \tau_{xy} & \tau_{yy} & \tau_{zy} & u\tau_{xy}+v\tau_{yy}+w\tau_{zy}+\dfrac{\kappa}{(\gamma-1)\,PrM_f^2}T_y \end{bmatrix}^T, \\[2mm]
\mathbf{H}^v &= \begin{bmatrix} 0 & \tau_{xz} & \tau_{yz} & \tau_{zz} & u\tau_{xz}+v\tau_{yz}+w\tau_{zz}+\dfrac{\kappa}{(\gamma-1)\,PrM_f^2}T_z \end{bmatrix}^T.
\end{aligned} \tag{5}$$

ρ, u, v, w, p, and T are the density, velocities, pressure, and temperature respectively. The specific total energy is $\rho e = p/(\gamma-1) + \frac{1}{2}\rho(u^2 + v^2 + w^2)$ and the system is closed by the equation of state,

$$p = \frac{\rho T}{\gamma M_f^2}. \tag{6}$$

All quantities are non-dimensionalized with respect to a problem specific reference length, velocity, density, and temperature yielding the non-dimensional Reynolds number, Re_f and Mach number, M_f.

We approximate the system, (1), with a discontinuous Galerkin spectral element method (DGSEM). Details can be found in [10, 11] and will not be discussed here.

IV. Setup

The flow over a NACA 65(1)-412 airfoil is simulated in two dimensions at a chord-based Reynolds number of $Re_c = 2 \times 10^4$ and a free-stream Mach number of $M = 0.3$. At this Mach number, the compressibility effect on the pressure coefficient are expected to be of the order of 5% in relation to incompressible flow, according to the Prandtl-Glauert correction $C_{p,M}/C_{p,i} = 1/\sqrt{1-M^2}$. A Prandtl number of $Pr = 0.72$, Sutherland constant $R_T = S/T_f = 110/200$, and ratio of specific heats $\gamma = 1.4$ are chosen in accordance with Nelson [12].

The Navier-Stokes equations are solved using a discontinuous Galerking spectral element method (DGSEM) [10]. The conservative variables (2) are spatially approximated on a Nth order polynomial basis and collocated on Legendre-Gauss quadrature nodes. A fouth-order explicit Runge-Kutta adaptive time-stepping scheme [13] is used with time step sizes ranging between $8.2 \times 10^{-6} \le \Delta t \le 1.3 \times 10^{-5}$. A Riemann solver is used to sort out the characteristics
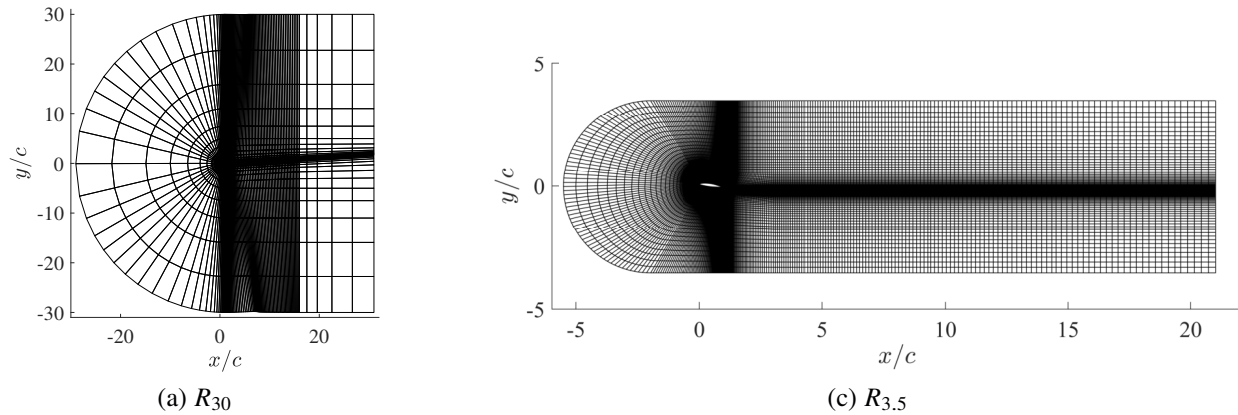
3

(a) R_{30}

(c) $R_{3.5}$

Fig. 1 Overview of computational domains: (a) Large domain with boundaries 30 chord lengths away from airfoil (R_{30}). (b) Narrow domain with boundaries 3.5 chord lengths away ($R_{3.5}$) and airfoil at incidence of $8°$. Only elements without interior Gauss nodes are shown.

at all boundaries [14, 15]. To account for the curvature of the airfoil, the boundary elements are curved and fitted to a spline representing the airfoil's surface according to Nelson et al. [16].

To model the flow in confined geometries, such as the test section of a wind tunnel, a narrow computational domain with transverse boundaries at $\pm 3.5c$ and wake length of 20 chord lengths is chosen. For the NACA 65(1)-412 at $4°$ and $8°$ incidence, the geometric blockage ratio is 1.8% and 2.5%, respectively. The results are compared to reference solutions of free-stream simulations on a large domain with boundaries 30 chord lengths away from the wing.

The computational domains are presented in Fig. 1. In Fig. 1 (a), the large domain of the reference solution is plotted. The mesh consists of 3366 quadrilateral elements and has been shown to give a converged solution for a polynomial order of 12 at an inflow angle of $4°$ and Reynolds number $Re_c = 2 \times 10^4$ [16]. The domain is rapidly stretched towards the outflow boundary and pressure damping [15] is gradually increased from $x/c = 12$ to $x/c = 16$ to reduce spurious reflections from vortices entering the low-resolution region. Consistent with Nelson et al. [16], we use a polynomial order of $N = 12$ in simulations with angle of attack of $4°$ but a higher order of $N = 18$ for AOA = $8°$ to provide sufficient resolution at the airfoil's leading edge.

The computational grids used for simulations with higher blockage is given in Fig. 1(b) with the airfoil at $8°$ incidence. A similar domain is used for simulations at AOA = $4°$. 20,640 and 22,102 quadrilateral elements provide high resolution around the airfoil and along the wake and allow for computations at a lower polynomial order of $N = 6$. Free-stream conditions are used at the inflow and outflow boundaries, and a pressure damping layer of 5 chord lengths is employed to reduce spurious reflections from vortices leaving the domain. The transverse boundaries are set either as free-stream or slip-wall conditions and the airfoil surface is approximated as no-slip adiabatic wall.

All simulations are run for at least 50 convective time units to reach quasi-steady state and statistics are subsequently computed over 30 convective time units.

V. Results and Discussion

A. AOA = $4°$

The time-averaged streamline pattern and contours of the velocity $|\mathbf{u}|$ are presented in Fig. 2. At $4°$ incidence, the flow is characterized by the separation of the shear layer at mid-chord ($x/c = 0.5$) and formation of a long recirculation region without reattachment to the airfoil surface. Vortices shed periodically from the pressure and suction side and form a Von-Karman-type vortex street behind the wing. Details of the flow can be found in [16, 17].

Figure 3 shows plots of the instantaneous pressure coefficient in the range from $-0.1 < C_p < 0.1$ on the left, which corresponds to approximately 10% of the stagnation pressure coefficient. On the right panel, RMS values obtained from statistics over 30 convective time units are presented. All cases show pressure waves radiating from the airfoil's trailing edge, which in the case of free-stream boundaries freely leave the domain (Fig 3a,c), but are reflected when slip walls are used (Fig 3b). Most noticeably, the pressure reflections lead to wave interference that result in a *checkerboard* interference pattern upstream, as well as above and below of the wing. In the wake, the pressure wave fluctuations
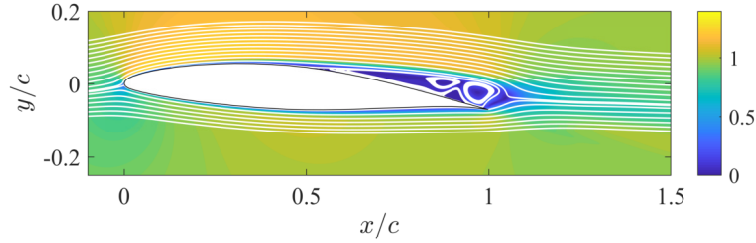
Fig. 2   Averaged absolute velocity contours |u| and streamlines at $Re_c = 2 \times 10^4$ and AOA = 4°.

appear in the form of elongated streamwise structures that travel downstream.

The wake flow is governed by a regular vortex street that extends approximately 5 (slip-wall), 7 (free-stream, $R_{3.5}$) and 9 (free-stream, R_{30}) chord lengths behind the wing before it becomes unstable and breaks up. The dispersion of the vortex street is quantified by analyzing the pressure coefficient RMS field in Fig. 3(b,d,f), which shows an earlier spread at slightly higher rate for the case with slip-wall boundaries as compared to free-stream simulations on the same domain. The pressure RMS field shows a similar wave interference pattern as observed in the instantaneous field, indicating that the interference pattern is reoccurring.

The impact of the wave reflections on the aerodynamic forces on the wing is assessed by means of lift, drag, pressure and skin friction coefficients in Fig. 4–6 and tabulated in Table 1. The time history of the lift and drag coefficients is governed by the shedding of vortices from the airfoil's trailing edge and shows fluctuations around a mean. The shedding is highly regular in case of free-stream conditions but becomes irregular if pressure waves are reflected from the boundaries. This pattern is reflected in the RMS values of the lift and drag coefficients, which increase from 5% to 6% of the time-averaged solution (Table 1). All cases show a dominant peak in lift spectrum at a Strouhal number of $St = fc/U_\infty = 2.8$ (see Fig. 5), but the pressure reflections in case of slip-wall boundaries result in several additional low-frequency peaks that point to the higher irregularity shown in Fig. 4.

Apart from the irregular fluctuations, the case with walls along the horizontal boundaries shows a 4% higher average lift coefficient than the equivalent simulation with free-stream conditions. When compared to the reference solution in the large domain, the difference reduces to 1%. The averaged drag force is affected by 1% at most. As shown in Fig. 6(a), this change is driven by a difference in the pressure coefficient at the leading edge: simulations with slip-wall boundaries show nearly identical values of C_p as given by the reference solution, whereas the narrow domain with free-stream boundaries deviates by 6%. The close proximity of the free-stream boundary appears to force the flow in the latter case.

RMS values of the pressure and skin friction coefficients are presented in Fig. 6(c–d). While both free-stream solutions show an identical RMS pattern, the slip-wall boundaries show increased fluctuation levels towards the trailing edge and point to the irregular vortex shedding pattern presented in Fig. 4. Notably, the pressure coefficient RMS of the slip-wall case shows a local minima at $x/c = 0.3$ and is 37% lower than compared to the free-stream solutions. While this result seems surprising at first, given the overall high levels of pressure fluctuations in the domain, the RMS(C_p) contours in Fig. 3(d) show a distinct interference pattern with a narrow region of low levels ranging from the airfoil's suction side vertically to the upper wall boundary. The reoccurring interference of pressure waves can therefore be attributed to the local minima 6(c). The RMS plots reveal another effect: although the averaged skin friction distribution is nearly identical (Fig. 6b), fluctuation levels at the asymptotic separation point, i.e. the time-averaged zero-skin-friction point, are actually reduced by 15% for the case with slip-walls as compared to the free-stream boundaries. This effect can be attributed to local minima in pressure fluctuations upstream of the separation point, as discussed previously. Impinging pressure waves from the boundary have therefore only little, if any, effect on the stability of the separated shear layer. Although the pressure reflections perturb the regularity of the vortex shedding, they do not induce a large-scale instability in the separated shear layer.

5

(a) C_p, free-stream $R_{3.5}$

(b) RMS(C_p), free-stream $R_{3.5}$

(c) C_p, slip-wall $R_{3.5}$

(d) RMS(C_p), slip-wall $R_{3.5}$

(e) C_p, free-stream R_{30}

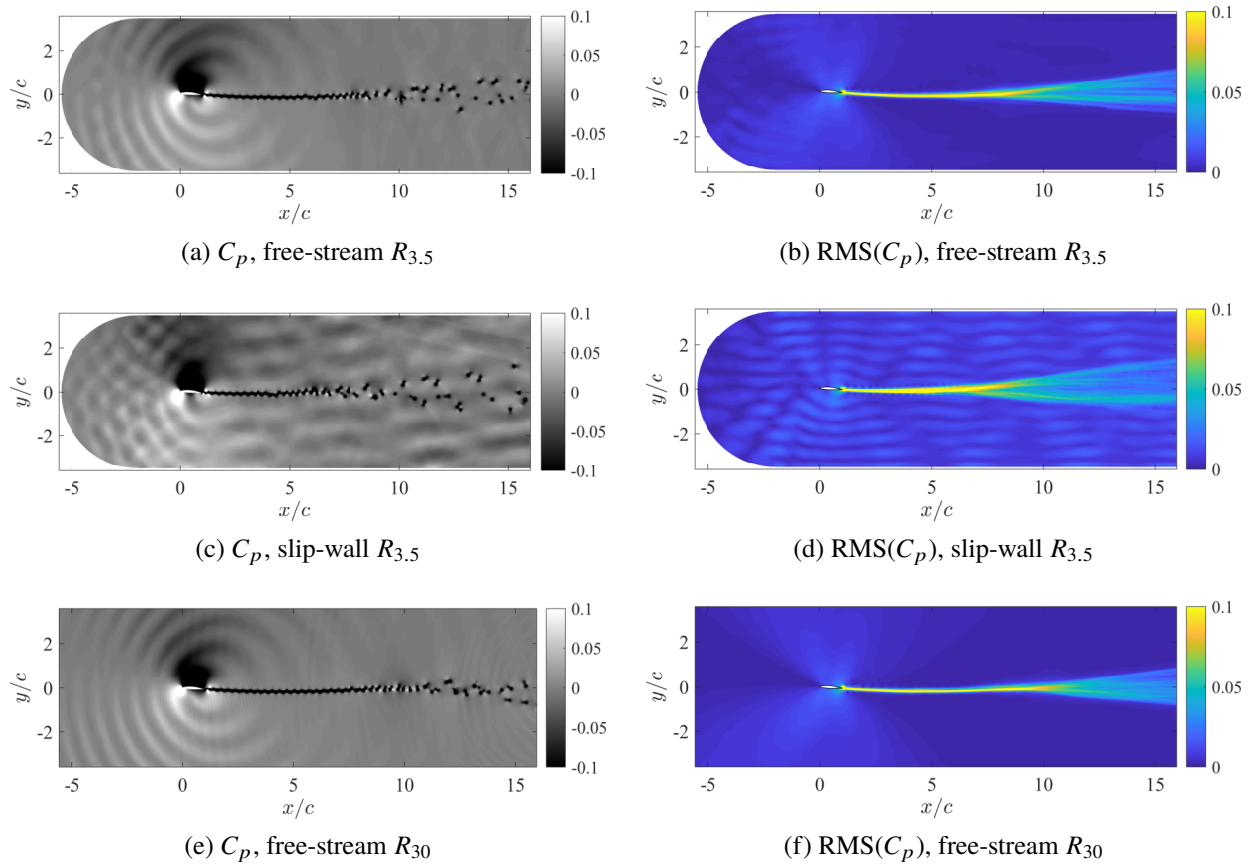(f) RMS(C_p), free-stream R_{30}

Fig. 3 Instantaneous pressure coefficient and corresponding RMS values in the wake of two-dimensional simulations for free-stream and slip-wall boundaries. $R_{3.5}$ and R_{30} correspond to to the vertical height of the domain size. AOA = 4°.
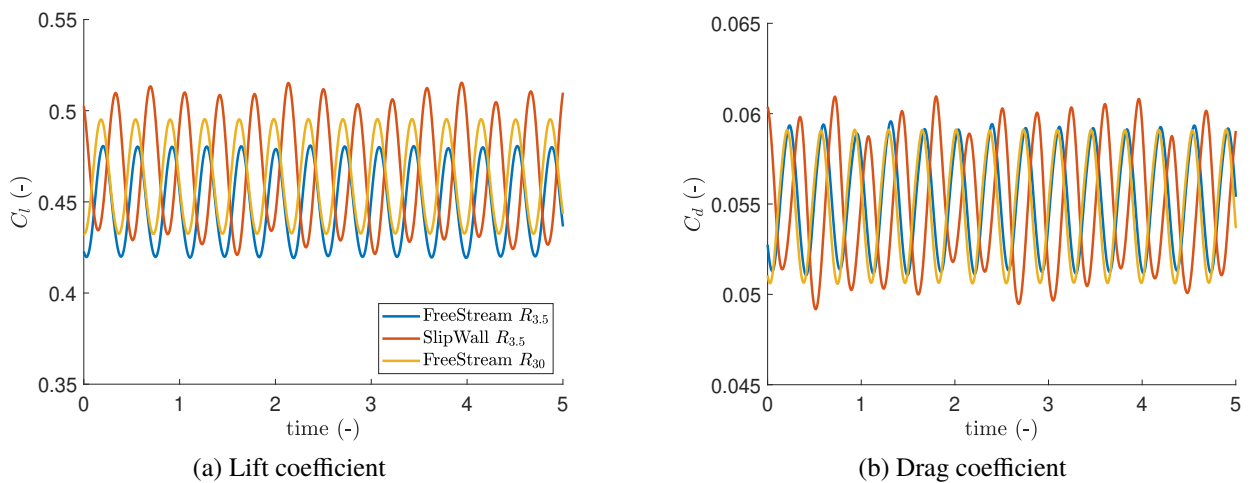

(a) Lift coefficient

(b) Drag coefficient

Fig. 4 Lift and drag coefficients over 5 convective time units for free-stream and slip-wall boundaries. AOA = 4°.

6

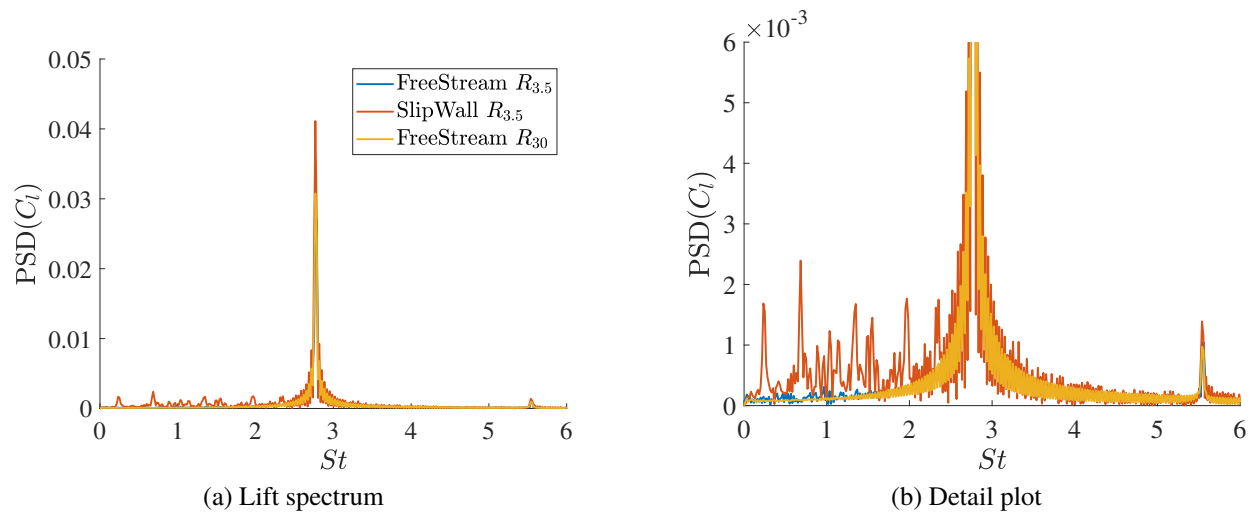(a) Lift spectrum

(b) Detail plot

Fig. 5   Energy spectrum of the lift coefficients over 30 convective time units for free-stream and slip-wall boundary. (a) Full spectrum and (b) detail plot. AOA = 4°.
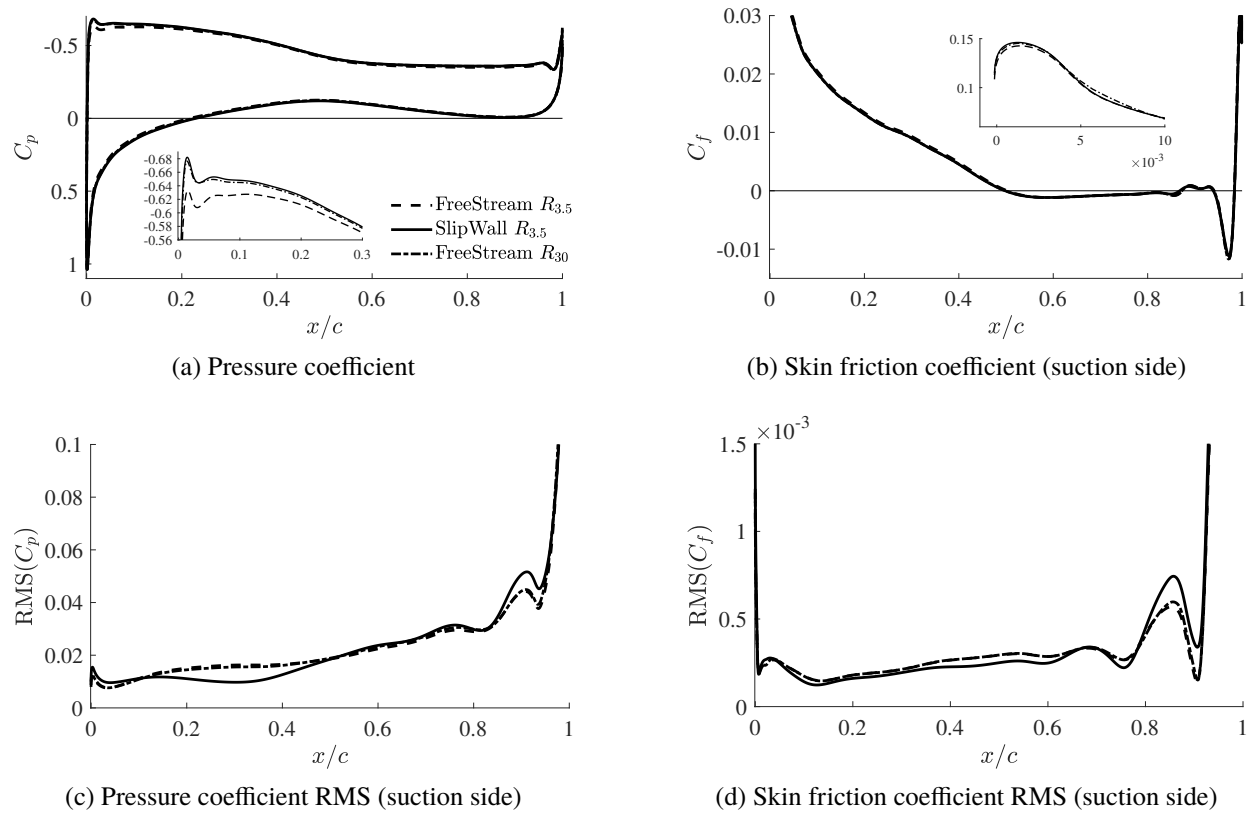

(a) Pressure coefficient

(b) Skin friction coefficient (suction side)

(c) Pressure coefficient RMS (suction side)

(d) Skin friction coefficient RMS (suction side)

Fig. 6   Time-averaged pressure (a) and skin friction (b) coefficients for free-stream and slip-wall boundary. RMS values for suction side given in (c) and (d). AOA = 4°.

7

Table 1   Lift and drag coefficients for AOA = 4°.

Boundary	$\bar{C}_l$	$C_{l,rms}$	$C_{l,rms}/\bar{C}_l$	$\bar{C}_d$	$C_{d,rms}$	$C_{d,rms}/\bar{C}_d$
Free-stream $R_{3.5}$	0.449	0.022	4.8%	0.055	0.0028	5.1%
Slip-wall $R_{3.5}$	0.468	0.030	6.3%	0.055	0.0033	6.1%
Free-stream R_{30}	0.463	0.022	4.8%	0.055	0.0029	5.4%
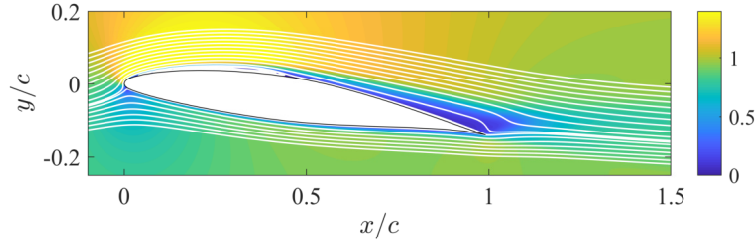
Fig. 7 Averaged velocity contours |u| and streamlines at $Re_c = 2 \times 10^4$ and AOA = 8°.

B. AOA = 8°

At 8° incidence, the separation point of the shear layer has moved to the leading edge of the airfoil and a laminar separation bubble (LSB) has formed (Fig. 7). As the separated shear layer becomes unstable (Kelvin-Helmholtz instability), the unsteady shedding of vortices results in the reattachment of the streamlines in the averaged flow field. Contrary to the flow at AOA = 4°, the reattachment downstream of the LSB leads to pressure recovery towards the trailing edge and the reduction of form drag. This state is thereby characterized by high lift and low drag forces [18].

The instantaneous pressure fields are presented on the left in Fig. 8 and the corresponding RMS fields from flow statistics over 30 convective time units are shown on the right. The flow in the narrow ($R_{3.5}$) domain with free-stream conditions along the outer horizontal boundaries has developed a narrow vortex street in the wake of the airfoil which only slowly disperses approximately seven chord lengths behind the wing (Fig. 8a–b). The pressure fields show a notable bending of the wake as vortices are initially forced in an upward motion before they move back to the centerline and advect horizontally towards the domain exit. With slip walls along the horizontal boundaries, the wake shows a highly irregular pattern with a much increased spreading rate. Although a general trend of the upward motion of the vortices is still present, they no longer follow the same distinct pattern observed in the computations with free-stream boundaries on the narrow domain. Surprisingly, the reference solution of the flow in the large domain (Fig. 8e–f) is governed by similar wake dynamics as found in the case with slip walls, as the wake shows an irregular pattern of vortex shedding, even though pressure waves can freely leave the domain. This result indicates that the proximity of the free-stream condition in the $R_{3.5}$ domain has a strong impact on the solution.

The regularity of the respective wakes is reflected in the time history of the lift and drag coefficients (Fig. 9 and Table 2). The slip-wall computations show a large increase in the fluctuation levels of the aerodynamic forces that reach 20% of the time-averaged drag coefficient and 7% of the lift. The corresponding spectra are plotted in Fig. 10. In case of the small domain with free-stream boundaries, the spectrum shows two distinct peaks: a dominant peak at a Strouhal number of $St = 2.2$ and a small peak at twice that frequency. The other two cases are characterized by a broad spectrum with several peaks in accordance with the chaotic vortex shedding. The spectrum of the case with slip walls has an overall higher energy content, corresponding to the higher amplitude of the force oscillations shown in Fig. 9.

The force fluctuations, driven by the vortex shedding over the airfoil and the trailing edge, indicate that the deviations of the wake shapes derive from differences in the generation of vortices from the separated shear layer over the wing. Instantaneous plots of the vorticity, pressure and skin-friction coefficients are shown in Fig. 11 from simulations in the narrow domain ($R_{3.5}$). The figures demonstrate that a strong adverse pressure gradient at the leading edge of the airfoil leads to the separation of the shear layer in both cases. As the separated flow becomes subject to Kelvin-Helmholtz (K-H) instability, the shear layer rolls up into right-turning vortices (blue). While the bottom shear layer remains attached, it forms a strong left turning vortex (yellow) as it sheds from the trailing edge and interacts with vortices from the suction side. The instantaneous plots (Fig. 11a–b) show that in the case of free-stream boundaries, a total of three vortices are present on the suction side, as indicated by local minima in the pressure coefficient. If the flow is confined between slip-wall boundaries, however, the vorticity and pressure plots indicate that the number of vortices has increased to five.

The difference in the vortex shedding pattern, driven by the instability of the separated shear layer, is clearly reflected in the time-averaged pressure and skin friction distributions in Fig. 12(a–b). At the leading edge, the pressure coefficient shows a difference of 5% between the cases, where the simulation on the narrow domain with free-stream conditions yields a distinctly lower value than the other two cases. This effect was reversed for the flow at 4° incidence, where the narrow domain with free-stream conditions lead to a higher pressure. Consistently, the pressure distributions of the flow between slip walls and the R_{30} reference solution match closely.

The skin-friction coefficient, on the other hand, displays larger deviations throughout the cases and indicate different sizes of the laminar separation bubble, based on zero-crossings of the wall shear stress. Most noticeably, the LSB ranges
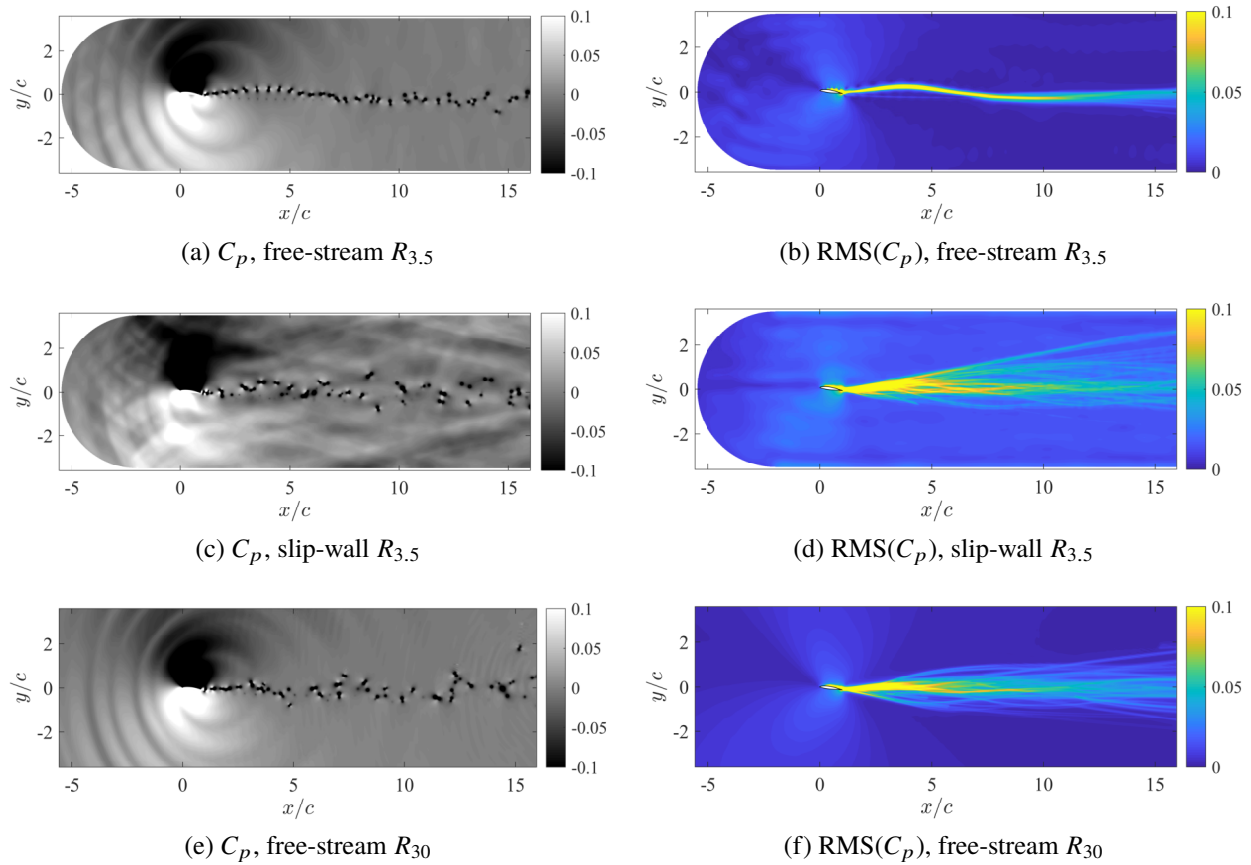
(a) C_p, free-stream $R_{3.5}$

(b) RMS(C_p), free-stream $R_{3.5}$

(c) C_p, slip-wall $R_{3.5}$

(d) RMS(C_p), slip-wall $R_{3.5}$

(e) C_p, free-stream R_{30}

(f) RMS(C_p), free-stream R_{30}

Fig. 8 **Instantaneous pressure coefficient and corresponding RMS values in the wake of two-dimensional simulations for free-stream and slip-wall boundaries.** $R_{3.5}$ **and** R_{30} **correspond to to the vertical height of the domain size. AOA = 8°.**
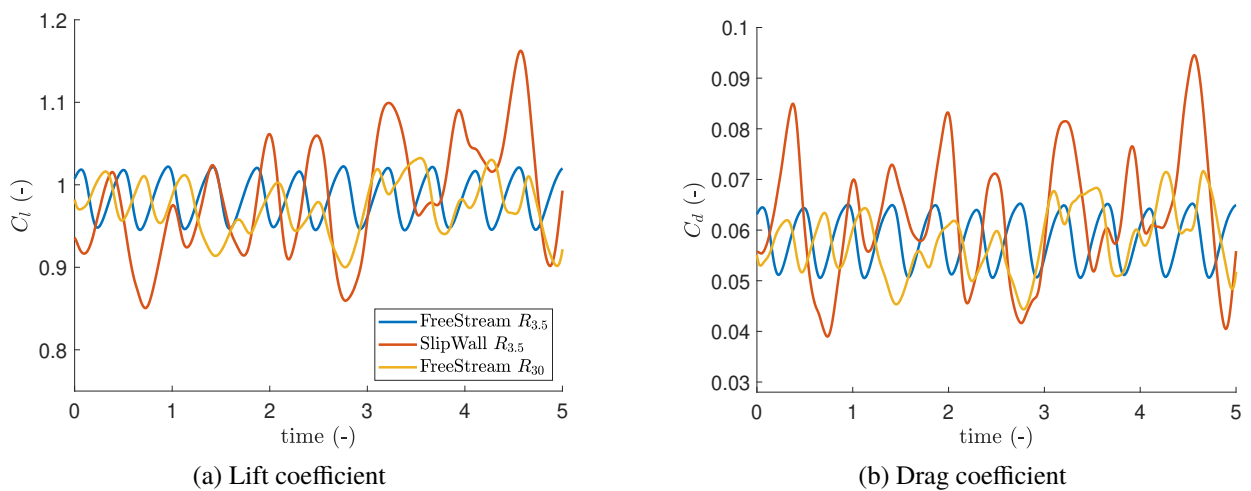

(a) Lift coefficient

(b) Drag coefficient

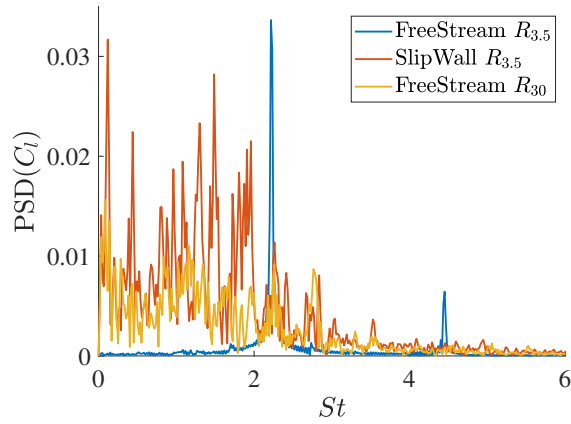**Fig. 9** **Lift and drag coefficients over 5 convective time units for free-stream and slip-wall boundary. AOA = 8°.**

Fig. 10   Energy spectrum of the lift coefficients over 30 convective time units for free-stream and slip-wall boundary. AOA = 8°.

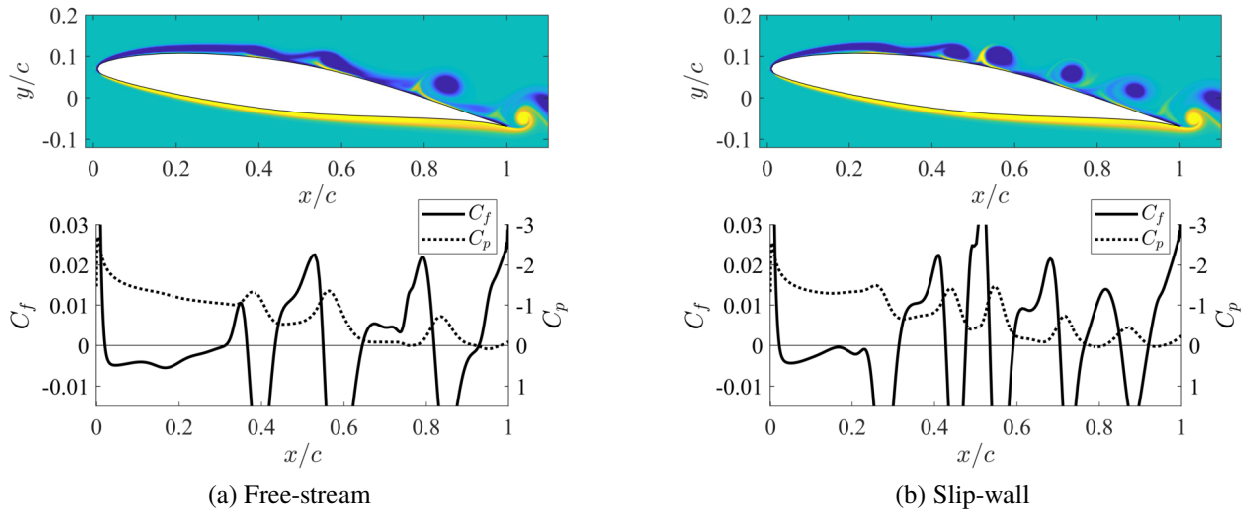(a) Free-stream

(b) Slip-wall

Fig. 11   Instantaneous plots of vorticity, pressure and skin friction coefficients on the suction side for free-stream (a) and slip-wall boundary (b). Domain: $R_{3.5}$**. AOA = 8°.**

(a) Pressure coefficient

(b) Skin friction coefficient (suction side)

(c) Pressure coefficient RMS (suction side)

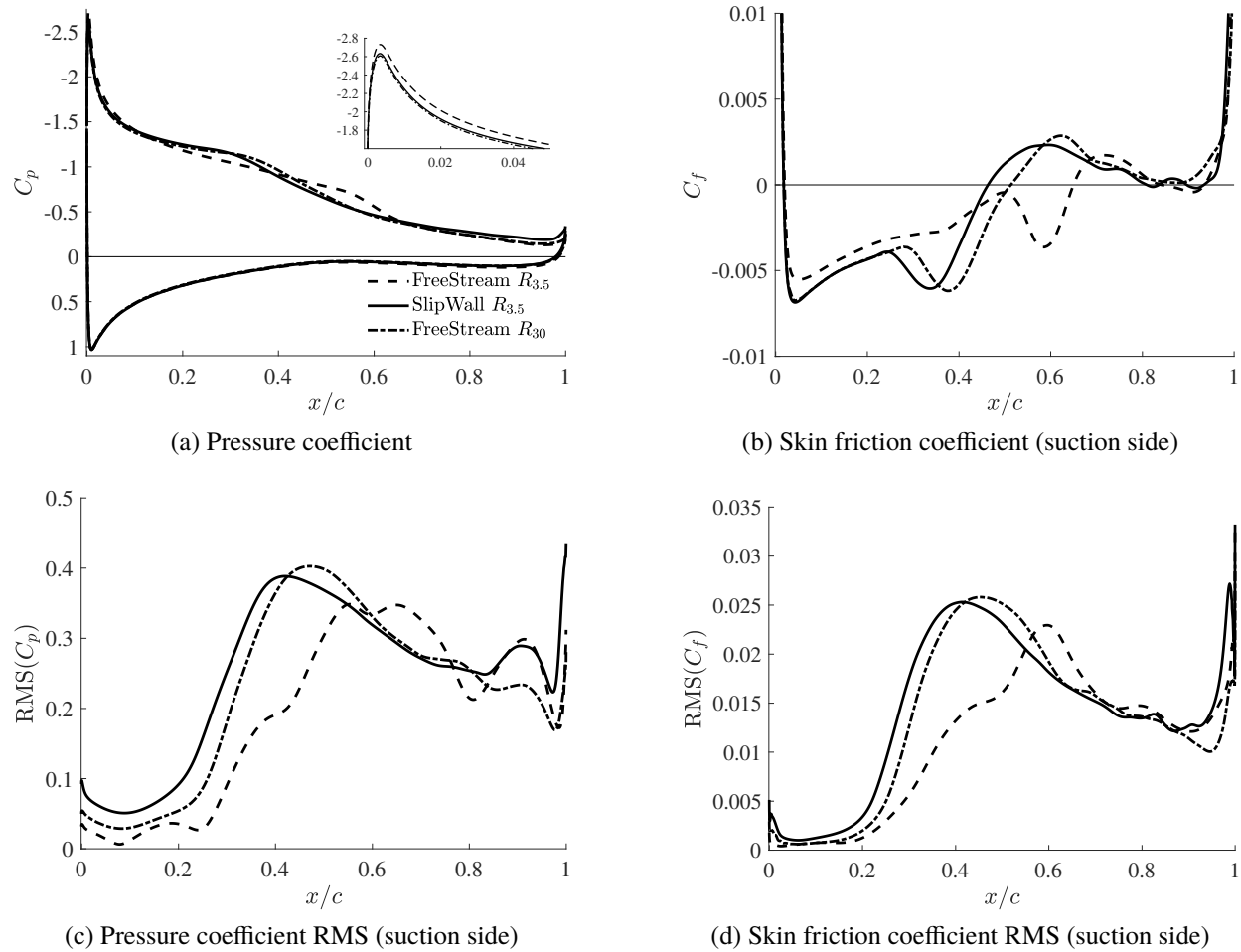(d) Skin friction coefficient RMS (suction side)

Fig. 12   Time-averaged pressure and skin friction coefficients for free-stream and slip-wall boundary. AOA = $8°$.

from the leading edge until $x/c = 0.46$ for free-stream boundaries and $x/c = 0.65$ for slip walls on the narrow domain (Fig. 12b). Corresponding to the local minima of C_f upstream of the reattachment point, the pressure distributions indicate a similar shift of the local dent.

The large differences of the flow topology in the case of free-stream boundaries in the narrow $R_{3.5}$ domain as compared to the other two solutions suggests that the proximity of the boundaries significantly forces the flow and results should be interpreted carefully. Comparing the averaged solutions of the flow between wall boundaries and the reference solution in the large domain, the pressure reflections result in a reduction of the LSB length by approximately $0.05c$ or 9% and approximately 70% higher levels of fluctuations in the bubble. As the suction-side vortices are generated by a K-H instability in a strong adverse pressure gradient, their formation is accelerated by perturbations from reflected pressure waves impinging on the shear layer and resulting in the shortened bubble length and higher levels of fluctuations within the LSB. As a result, the aerodynamic forces show a much higher irregularity than for the case of free-stream boundary conditions (Table 2).

In laminar separation bubbles, the stability is linked to the reverse flow levels where Alam and Sandham [19] have shown that a reverse flow velocity U_R of 15-20% of the local boundary layer edge velocity is necessary to develop an absolute stability. For values below this threshold, the instability is assumed to be of convective nature or linked to three-dimensional modes [20, 21]. For the flow over NACA 0012 at $Re_c = 5 \times 10^4$, Jones et al. [7] report reverse flow levels of 15.3% for three-dimensional DNS and 22.2% for two-dimensional simulation. Because the reverse flow levels quantifying the tendency of the flow to become unstable and transition to turbulence, we evaluate the time-averaged tangential velocity component within the LSB and normalize it by the local boundary layer edge velocity (Fig. 13). The boundary layer edge is determined according to the methodology used by Uranga et al. [22], where irrotational flow is

Table 2   Lift and drag coefficients for AOA = 8°.

Boundary	$\bar{C}_l$	$C_{l,rms}$	$C_{l,rms}/\bar{C}_l$	$\bar{C}_d$	$C_{d,rms}$	$C_{d,rms}/\bar{C}_d$
Free-stream $R_{3.5}$	0.984	0.026	2.6%	0.058	0.0049	8.5%
Slip-wall $R_{3.5}$	0.976	0.067	6.9%	0.060	0.0120	19.9%
Free-stream R_{30}	0.963	0.038	3.9%	0.057	0.0073	12.7%

Table 3   Normalized reverse flow velocities U_R. AOA = 8°.

Free-stream R_{30}	Slip-wall $R_{3.5}$	Free-stream $R_{3.5}$
6.2%	5.1%	1.2%

assumed outside the boundary layer and the vorticity and the vorticity gradient being below a threshold.

The values of the reverse flow are tabulated in Table 3. While all reverse flow levels are well below 10%, the simulations conducted on the large (R_{30}) computational domain shows the highest recirculating velocity magnitude of 6.2%. The very low level of 1.2% for the case of free-stream boundaries in the $R_{3.5}$ domain provides an explanation for the regularity of the aerodynamic forces and the vortex street: the proximity of the upper and lower free-stream boundaries in the $R_{3.5}$ domain force the flow towards the horizontal unit velocity vector, thereby reducing the height of the LSB at the leading edge and suppressing the reverse flow. This effect is still noticeable for the simulation with slip-walls but to a lower degree because the strongly increased levels of pressure fluctuations induce instabilities in the separated shear layer at the leading edge that lead to the formation of vortices which in turn induce reverse flow. Furthermore, the boundary does not force the flow to the free-stream value at the domain edges, but only impose a zero vertical flow component.

The different sizes of the LSB are also reflected in the boundary layer displacement thickness δ^*, the momentum thickness θ, and consequently the shape factor $H = \delta^*/\theta$ (see Fig. 14). The lower bubble height for the case of free-stream boundaries in the $R_{3.5}$ domain results in a reduced displacement thickness accordingly and the peak in the shape factor, which indicates the transition point of the flow [22], is rather flat. The other two case show stronger peaks in H, with the large domain again having the higher value over the small domain with slip walls. Likely, the reason is that the bubble height is slightly reduced in the case of the small domain as the outer boundaries strictly enforce horizontal flow and thereby limit the displacement of the flow more than in a large domain.

The comparison of the airfoil flow in a narrow domain with walls to the free-stream case shows that there are two mechanisms that induce and suppress instabilities: the pressure reflections from the walls induce instabilities within the separated shear layer, but the condition of horizontal flow at the boundaries also limits the displacement of the streamlines and result in a smaller bubble height. Given all the differences in the flow patterns, including deviations in the LSB length of nearly 30%, as well as substantial changes in the wake topologies, it is somewhat surprising that the lift coefficient is affected by merely 2% and the drag by 5% (Table 2).

VI. Conclusion

The impact of pressure reflections on the instantaneous and mean properties of the transitional flow around a NACA 65(1)-412 airfoil has been evaluated in a domain with horizontal slip-wall boundaries. For angles of attack of 4° and 8°, the flow is computed with horizontal slip walls and compared to solutions with free-stream boundaries on the same domain, as well as free-stream computations on a large domain.

At 4° incidence, the natural flow is characterized by laminar separation at mid-chord without reattachment and with highly regular vortex shedding from the trailing edge. The interaction of reflected pressure waves with the airfoil and the wake results in a higher irregularity of the lift and drag force, as well as an earlier dispersion of the vortex street, but shows only small differences in the time-averaged pressure and skin-friction coefficients over the wing. At an intermediate angle of attack of 8°, a laminar separation bubble has formed at the leading edge and sheds vortices over the wing. The receptivity of this bubble to disturbances is much higher than the recirculation region at 4° and now distinctly affects the flow topology and LSB size. Although the reflected pressure waves traveling across the domain are

(a) Free-stream (R_{30})

(b) Slip-wall ($R_{3.5}$)
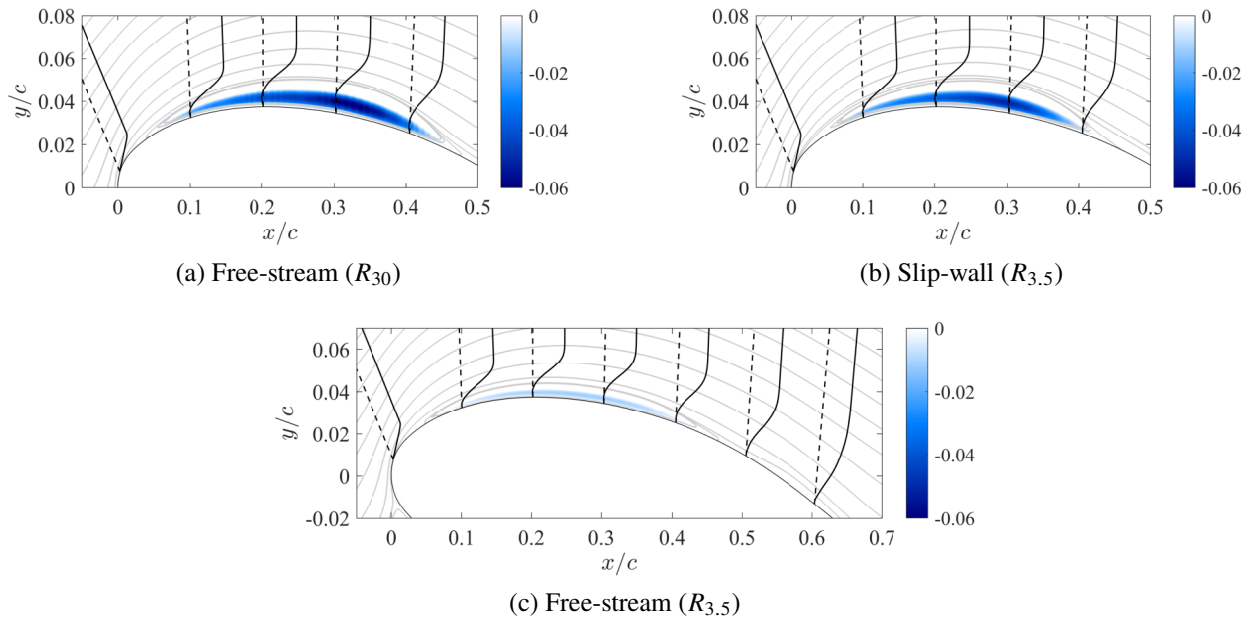
(c) Free-stream ($R_{3.5}$)

Fig. 13   Contours of averaged tangential flow normalized by the local velocity magnitude at the boundary layer edge. Streamlines in gray, normal velocity profiles in black. Plots are not to-scale to aid visibility. AOA = 8°.

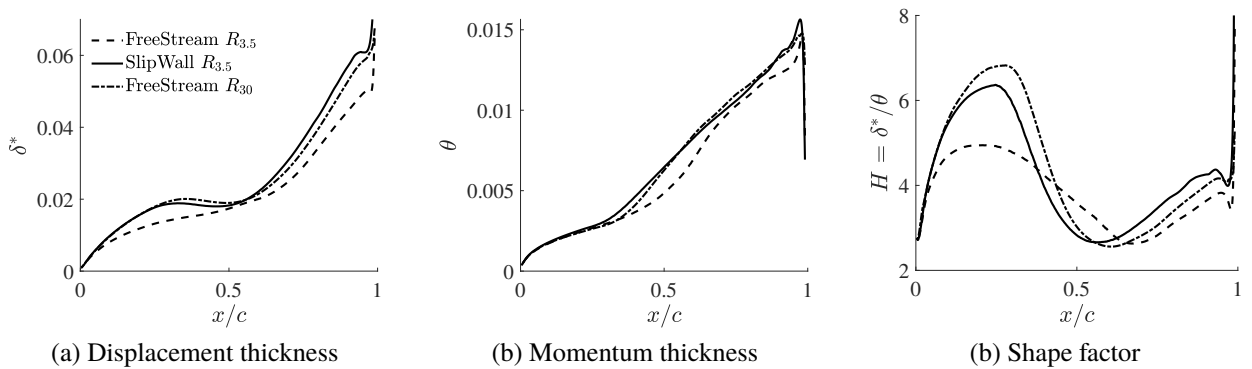(a) Displacement thickness

(b) Momentum thickness

(b) Shape factor

Fig. 14   Comparison of displacement thickness δ^*, momentum thickness θ, and the shape factor $H = \delta^*/\theta$ for free-stream and slip-wall boundary. AOA = 8°.

14

of the order of 10% of the stagnation pressure, the integrated forces over the airfoil differ by 5% at most. If the objective of a simulation is to determine flow structures and forces with maximum accuracy for a given computational cost then the wall boundary effects must be considered and perhaps treated. especially if the results of either integrated forces or flow structure distribution are to be compared with experiment where boundary effects are inescapable.

Acknowledgments

References

[1] Tank, J., Smith, L., and Spedding, G. R., "On the possibility (or lack thereof) of agreement between experiment and computation of flows over wings at moderate Reynolds number," *Interface Focus*, Vol. 7, No. 1, 2017, p. 20160076.

[2] Lissaman, P. B. S., "Low-Reynolds-Number Airfoils," *Annual Review of Fluid Mechanics*, Vol. 15, No. 1, 1983, pp. 223–239. https://doi.org/10.1146/annurev.fl.15.010183.001255.

[3] Herrig, L. J., Emery, J. C., and Erwin, J. R., "Systematic two-dimensional cascade tests of NACA 65-series compressor blades at low speeds," Naca technical note 3916, 1951.

[4] Wright, L. C., "Blade selection for a modern axial-flow compressor," Nasa conference proceedings, 1974.

[5] Tank, J., Klose, B. F., Jacobs, G., and Spedding, G. R., "Computer and laboratory studies on the aerodynamics of the NACA 65(1)-412 at Reynolds number 20 000," Aiaa scitech 2019 forum, 2019.

[6] Moin, P., and Mahesh, K., "Direct Numerical Simulation: A Tool in Turbulence Research," *Annual Review of Fluid Mechanics*, Vol. 30, No. 1, 1998, pp. 539–578.

[7] Jones, L. E., Sandberg, R. D., and Sandham, N. D., "Direct numerical simulations of forced and unforced separation bubbles on an airfoil at incidence," *Journal of Fluid Mechanics*, Vol. 602, 2008, pp. 175–207.

[8] Jones, L. E., Sandberg, R. D., and Sandham, N. D., "Stability and receptivity characteristics of a laminar separation bubble on an aerofoil," *Journal of Fluid Mechanics*, Vol. 648, 2010, pp. 257–296.

[9] Zhang, W., Cheng, W., Gao, W., Qamar, A., and Samtaney, R., "Geometrical effects on the airfoil flow separation and transition," *Computers & Fluids*, Vol. 116, 2015, pp. 60 – 73.

[10] Kopriva, D. A., *Implementing Spectral Methods for Partial Differential Equations*, Springer, New York, 2009.

[11] Klose, B. F., Jacobs, G. B., and Kopriva, D. A., "Assessing standard and kinetic energy conserving volume fluxes in discontinuous Galerkin formulations for marginally resolved Navier-Stokes flows," *Computers & Fluids*, Vol. 205, 2020, p. 104557. https://doi.org/https://doi.org/10.1016/j.compfluid.2020.104557.

[12] Nelson, D. A., "High-Fidelty Lagrangian Coherent Structures Analysis and DNS with Discontinuous-Galerkin Methods," PhD Thesis, University of California, San Diego in conjuction with San Diego State University, San Diego, CA, Month unknown 2015. Http://escholarship.org/uc/item/2cv4f732.

[13] Carpenter, M. H., and Kennedy, C. A., "A fourth-order 2N-storage Runge-Kutta scheme," NASA TM 109112, Jun. 1994.

[14] Kopriva, D. A., "A staggered-grid multidomain spectral method for the compressible Navier-Stokes equations," *J. Comp. Phys.*, Vol. 143, 1998, pp. 125–158.

[15] Jacobs, G. B., Kopriva, D. A., and Mashayek, F., "A comparison of outflow boundary conditions for the multidomain staggered-grid spectral method," *Num. Heat Transfer, Part B*, Vol. 44, 2003, pp. 225–251.

[16] Nelson, D. A., Jacobs, G. B., and Kopriva, D. A., "Effect of Boundary Representation on Viscous, Separated Flows in a Discontinuous-Galerkin Navier-Stokes Solver," *Theoretical Computational Fluid Dynamics*, Vol. 30, 2016, pp. 363–385.

[17] Klose, B. F., Serra, M., and Jacobs, G. B., "Kinematics of Lagrangian Flow Separation in External Aerodynamics," *AIAA Journal*, Vol. 58, No. 5, 2020, pp. 1926–1938.

[18] Klose, B. F., Jacobs, G. B., Tank, J., and Spedding, G., "Low Reynolds number airfoil aerodynamics: three different flow patterns within an angle of attack range of four degrees," *AIAA AVIATION Forum*, 2018.

[19] Alam, M., and Sandham, N. D., "Direct numerical simulation of 'short' laminar separation bubbles with turbulent reattachment," *Journal of Fluid Mechanics*, Vol. 410, 2000, pp. 1–28. https://doi.org/10.1017/S0022112099008976.

[20] Theofilis, V., "Global Linear Instability," *Annual Review of Fluid Mechanics*, Vol. 43, 2011, pp. 319–352.

[21] Marxen, O., Lang, M., and Rist, U., "Vortex formation and vortex breakup in a laminar separation bubble," *Journal of Fluid Mechanics*, Vol. 728, 2013, pp. 58–90. https://doi.org/10.1017/jfm.2013.222.

[22] Uranga, A., Persson, P.-O., Drela, M., and Peraire, J., "Implicit Large Eddy Simulation of transition to turbulence at low Reynolds numbers using a Discontinuous Galerkin method," *International Journal for Numerical Methods in Engineering*, Vol. 87, 2011, pp. 232–261.